



# Flexure-based 60 degrees stroke actuator suspension for a high torque iron core motor

M. Naves\*, M. Nijenhuis, W.B.J. Hakvoort, D.M. Brouwer

Chair of Precision Engineering, University of Twente, P.O. Box 217, 7500AE Enschede, The Netherlands

## ARTICLE INFO

### Keywords:

Compliant mechanism  
Torque motor  
Actuator  
Flexure mechanism  
Large stroke

## ABSTRACT

For the actuation of flexure-based precision systems direct drive actuators are used to allow for precise manipulation. For this purpose, often iron-less direct drive actuators are used which do not suffer from parasitic magnetic forces. In contrast, actuators with iron core can provide a higher power density, but require high off-axis stiffness normally too demanding for flexure-based mechanisms, especially when combined with a large range of motion. In this paper, a flexure-based suspension for an iron core direct drive torque motor with a range of motion of 60 degrees and a maximum output torque of 55 Nm is presented. The system provides the required high off-axis stiffness (more than 1000 N/mm) and is able to withstand the high pull-in forces caused by the iron core over the full range of motion. Furthermore, the design is made robust by limiting the deflections in the support directions, effectively rerouting excess forces from the flexures into the frame parts. Experimental validations confirm the high support stiffness and show that the system is able to withstand high actuation and reaction forces. Due to the friction-free mechanical design, only the current noise from the motor driver limits the stand-still performance and the repeatability of the system, resulting in a RMS positioning error of 1.1  $\mu$ rad for an inertia of 0.066 kgm<sup>2</sup>.

## 1. Introduction

Hexapod robots are used for manipulation in up to six independent degrees of freedom [1]. Conventional systems consisting of traditional (rolling) bearings typically allow for a position accuracy down to a micrometer [2–4]. However, for precision applications such as optical alignment and micro assembly systems an accuracy well below one micrometer is required [5–7]. This can be achieved by eliminating all sources of play and friction in the joints to improve the determinism of the system [8–11], which in turn can be obtained by replacing the traditional bearings by flexure-based equivalents [12–15].

To maintain these deterministic properties in actuated robotic systems, the actuators of flexure-based precision systems should also be free of play and friction [16]. To this end, direct drive actuators can be used since they lack tribological contacts. Common Lorentz-type actuators such as voice coil [17], linear iron-less [18] or rotary iron-less (torque) motors [19] rely on a permanent magnetic field and coil windings (without iron core) to provide actuation forces. Due to the absence of the iron core, high parasitic magnetic forces are avoided [20]. However, the absence of the iron core also results in a reduced strength of the magnetic field and reduced thermal dissipation, which limit the maximum actuation force.

In contrast, Lorentz-type actuators with an iron core, in which the coils are mounted in an iron lamination stack, allow for an increased power density due to the high magnetic flux between the iron core and the permanent magnets [20,21]. This results in increased actuation forces given a similar size of the actuator. However, the increase in power density comes at the expense of parasitic magnetic forces in the drive direction (cogging) and perpendicular to the drive direction (pull-in). For rotational Lorentz-type actuators, these parasitic pull-in forces are proportional to the misalignment between the magnet track and iron core away from the equilibrium position located at the center, resulting in a destabilizing negative stiffness.

The challenge in using a flexure-based suspension is ensuring that the support stiffness and load capacity are sufficiently large to withstand the parasitic magnetic forces and reaction forces from the actuated system. This challenge is compounded for a large range of motion: when deformations increase, support stiffness and load capacity decrease, and the parasitic error motion of flexures increases [22–24]. Additionally, the non-linear nature of the elastic deformations of the flexures also results in parasitic error motions [25,26] that easily exceeds the alignment tolerances of typical actuators resulting in contact between the moving and stationary parts.

\* Corresponding author.

E-mail address: [m.naves@utwente.nl](mailto:m.naves@utwente.nl) (M. Naves).

<https://doi.org/10.1016/j.precisioneng.2020.02.001>

Received 6 November 2019; Received in revised form 11 January 2020; Accepted 1 February 2020

Available online 5 February 2020

0141-6359/© 2020 The Authors.

Published by Elsevier Inc.

This is an open access article under the CC BY-NC-ND license

(<http://creativecommons.org/licenses/by-nc-nd/4.0/>).

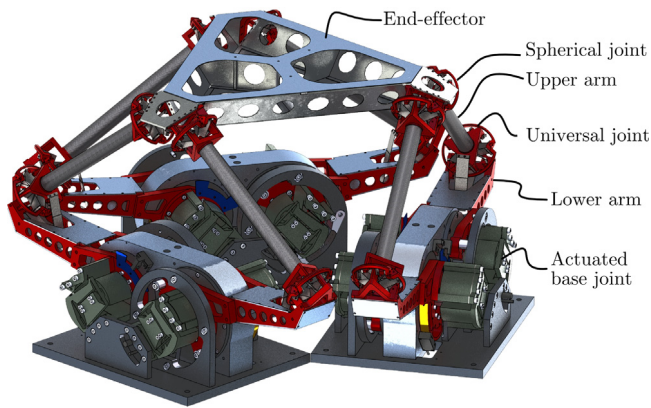


Fig. 1. Concept design of the 6RUS parallel manipulator (the T-Flex).

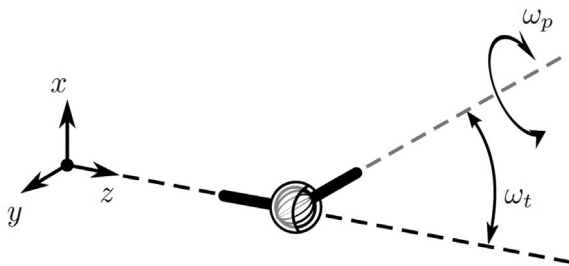


Fig. 2. Tilt ( $\omega_t$ ) and pan motion ( $\omega_p$ ) of a spherical joint.

In this paper, a flexure-based actuator suspension with 60 degrees range of motion for an iron core actuator is presented. It is designed to meet the requirements for a fully flexure-based large range of motion high precision hexapod, for which high actuation torque is needed. First, in Section 2, a brief description of the hexapod is provided to derive the requirements for the actuator and the flexure-based bearing construction. Next, in Section 3, the parasitic motion of three flexure-based cross-hinge candidate designs are compared and analyzed for the considered application. Furthermore, the individual designs of the cross hinges are numerically optimized in Section 4 in order to obtain the optimal design with respect to support stiffness in the load bearing directions. In Section 5, the influence of the pull-in forces on the flexure bearing is analyzed. In Section 6, a prototype design is presented and experimental validations are provided in Section 7.

## 2. System description

In this paper the design of the actuated base joints with a single rotational degree of freedom for a fully flexure-based 6RUS hexapod is considered. The hexapod consists of six arms, each made up of one actuated revolute joint at the base and a spherical and universal joint connected to each other via two links. A concept drawing of the hexapod is provided in Fig. 1. The hexapod design itself will be described in more detail in a future publication. Aim of the system is to pursue high positioning repeatability ( $< 100$  nm) combined with a large workspace ( $100 \times 100 \times 100$  mm) and high accelerations ( $> 5$  g).

The design of the flexure-based universal and spherical joints for the hexapod is given by the serial stacked folded leafspring design presented by Naves et al. [27]. The universal and spherical joints are designed to allow for 25 degrees tip-tilt motion, which describes the rotation angle of the directional axis ( $\omega_t$ , schematically illustrated in Fig. 2). Rotation around the directional axis for the spherical joint is given by pan motion ( $\omega_p$ ), which is limited to 10 degrees of rotation.

### 2.1. Requirements

Given the dimensions of the hexapod, the desired workspace and the range of motion of the spherical joints, a bi-directional range of motion of approximately 30 degrees is required for the actuated revolute base joints. Additionally, in order to allow for accelerations of the end-effector exceeding 5 g, to counteract gravity and to elastically deflect all joints, the required torque is specified at 40 Nm. To enable the targeted repeatability, the required rotational repeatability of the actuators is set at  $< 1$   $\mu$ rad.

### 2.2. Actuator selection

No suitable iron-less actuator is found to provide the required torque with an acceptable size or envelope. Therefore, we select an actuator with iron core, and settle for Tecnotion's direct drive iron-core torque motor (QTR-A-133-60) with an outer diameter of 133 mm [28], which allows for a continuous torque of 21.9 Nm and an ultimate torque of 55.5 Nm,<sup>1</sup> meeting the torque requirement.

The negative radial stiffness induced by the magnetic forces between the iron core and permanent magnets (pull-in) is approximately 350 N/mm and near constant over the range of the air gap (1 mm) between the rotor and the stator [29]. Furthermore, due to the moving magnet configuration, the actuator features a stationary coil without cables connected to any moving part, eliminating parasitic forces on moving parts by bending of cables.

## 3. Parasitic motion of revolute flexure joints

For commonly-used flexure joints for a single rotational degree of freedom, such as the cross-spring pivot consisting of two (or more) separate leafsprings [9,26], motion of the shuttle (in this case attached to the rotor) can be approximated by a circular motion around a fixed axis of rotation. However, for larger deflection angles, the motion path of the shuttle deviates significantly from this circular path as a consequence of the non-linear nature of the elastic deformations of the flexures. That deviation results in parasitic motion of the rotor which can easily exceed the required alignment tolerance of  $< 1$  mm between the rotor and the stator for the selected actuator. When also taking into account the negative stiffness induced by the permanent magnets and the reaction forces induced by accelerations, additional deformations will cause further deviation from its ideal circular trajectory resulting in additional parasitic motion.

In the next section, the motion characteristics of the cross-spring pivot [26], the cartwheel hinge [8,30] and the butterfly hinge [31] are compared for the purpose of selecting the optimal joint type. The effect of the negative radial stiffness and reaction forces are disregarded in order to allow for an analytical comparison between the hinge designs. The motion characteristics are compared in terms of their parasitic motion, which is defined as their deviation with respect to the ideal circular motion profile. The properties of the hinge designs including pull-in forces of the rotor is analyzed in more detail in Section 5.

### 3.1. Parasitic motion of the cross-spring pivot

For the traditional cross-spring pivot consisting of two (or more) individual leafsprings crossing at half their length, the dominant parasitic motion is in  $y$ -direction and provided by [32]

$$d_y = \frac{L}{12 \cos(\alpha)} \theta^2 \quad (1)$$

with  $L$  the length of the flexures,  $\theta$  the rotation angle of the shuttle and  $\alpha$  the relative angle between the leafsprings (schematically illustrated in Fig. 3).

<sup>1</sup> At ultimate torque the temperature of the coil increases by 20 °C/s. The maximum duration at which this torque can be maintained depends on thermal properties of the coils housing.

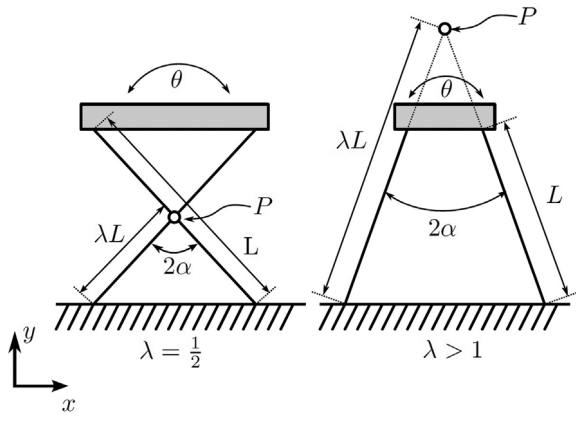


Fig. 3. Schematic overview of the cross-spring pivot with P indicating the location of the (initial) pivot axis,  $\lambda$  the relative location at which the flexures cross and  $\theta$  the rotation angle of the shuttle.

For a typical value of  $\alpha = 45^\circ$  and a maximum deflection angle of  $\theta = 30^\circ$ , the resulting parasitic motion is approximately  $L/31$ . As the maximum allowed parasitic motion is dictated by the design of the actuator, this implies a limit on the allowed length of the flexures to prevent contact between the rotor and stator. Therefore, ensuring a parasitic motion well below 1 mm requires short flexures. Consequently, the flexures also need to be thin to respect the stress limit for the flexures.

The parasitic motion of the cross-spring pivot can be greatly reduced by choosing  $\lambda = 1/2 \pm \sqrt{5}/6$ , with  $\lambda$  providing the relative location at which the flexures cross. For this specific value of  $\lambda$ , the second order contribution to the parasitic motion in  $y$ -direction is eliminated and the dominant contribution to the parasitic motion is now given by the smaller motion in  $x$ -direction instead, which is provided by [33]

$$d_x = \frac{\cot^2(\alpha)L}{141 \cos(\alpha)} \theta^3 \quad (2)$$

For  $\alpha = 45^\circ$  and  $\theta = 30^\circ$ , this results in a parasitic motion of approximately  $\frac{L}{695}$ , which provides a reduction of more than a factor of 20 compared to the traditional cross-spring pivot with  $\lambda = 1/2$  with the same dimensions. This strongly reduced parasitic motion does allow for longer flexures. However, the asymmetry also results in one flexure part to be short (approximately  $0.127L$ ), causing the bending stress due to deflection to be high, which in turn requires the thickness of the flexures to be small.

Furthermore, it has to be noted that the magnitude of the parasitic motion for this hinge design is more sensitive to deviations in the value of  $\lambda$ . For example, the shift in  $y$ -direction is provided by

$$d_y = -70 \frac{9\lambda^2 - 9\lambda + 1}{1050 \cos(\alpha)} L\theta^2 \quad (3)$$

for which the derivative with respect to  $\lambda$  is given by

$$\frac{\Delta d_y}{\Delta \lambda} = -70 \frac{18\lambda - 9}{1050 \cos(\alpha)} L\theta^2 \quad (4)$$

At  $\lambda = 1/2 + \sqrt{5}/6$  considering  $\alpha = 45^\circ$  and  $\theta = 30^\circ$ , this results in a sensitivity of

$$\Delta d_y \approx -\frac{1}{6} L\Delta\lambda \quad (5)$$

which is significant with respect to the obtained parasitic motion from Eq. (2) for already small values of  $\Delta\lambda$ . Therefore, this hinge design would require narrow alignment and manufacturing tolerances in order to actually realize this small magnitude for the parasitic motion.

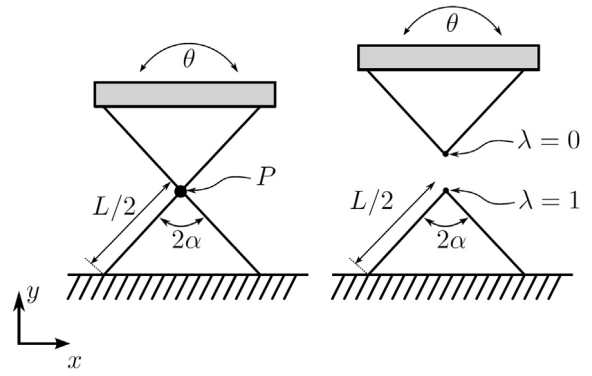


Fig. 4. Schematic overview of the cartwheel hinge with P indicating the location of the pivot axis and  $\theta$  the rotation angle of the shuttle. Note that for the cartwheel hinge the flexures are interconnected at point P, in contrast with the cross-spring pivot.

### 3.2. The cartwheel hinge

An alternative flexure-based design for a single rotational degree of freedom is provided by the cartwheel hinge, schematically illustrated in Fig. 4, which consists of two leafsprings intersecting at half their length. To evaluate the characteristics of the cartwheel hinge, the results from the earlier section can be used by considering the cartwheel hinge as a stacked arrangement of two cross-spring pivots with  $\lambda = 1$  and  $\lambda = 0$ . To obtain a similar footprint for the cross-spring pivot and the cartwheel hinge for a specific value of  $L$ , the flexure length of each flexure in the cartwheel hinge is given length  $L/2$ , schematically illustrated in Fig. 4. The resulting parasitic motion is then given by [34]

$$d_y = \frac{L}{63 \cos(\alpha)} \theta^2 \quad (6)$$

This effectively results in a parasitic motion of  $L/162$  for  $\alpha = 45^\circ$  and  $\theta = 30^\circ$ . Compared to the cross-spring pivot, this hinge suffers from an intermediate level of parasitic motion, inbetween the standard cross-spring pivot with  $\lambda = 1/2$  and the cross-spring pivot with minimal parasitic motion given  $\lambda = 1/2 \pm \sqrt{5}/6$ .

### 3.3. The butterfly hinge

A third design for a cross-hinge, which is known for its small parasitic motion due to the smart compounding of leafsprings, is provided by the butterfly hinge design. This hinge effectively consists of a stacked arrangement of four cross-spring pivots with coinciding rotation axes, schematically illustrated in Fig. 5. For this joint, parasitic motion of the first and fourth cross-spring pivot in the stacked arrangement is compensated for by opposed parasitic motion of the second and third cross-spring pivot. Therefore, parasitic motion is reduced resulting in [33]

$$d_y = \left( \frac{1}{\cos(\alpha_2)} - \frac{1}{\cos(\alpha_1)} \right) \frac{9\lambda^2 - 9\lambda + 1}{240} L\theta^2 \quad (7)$$

with  $\lambda > 1$  in order to prevent interference between the individual cross-spring pivots in the stacked arrangement and with  $\alpha_1$  and  $\alpha_2$  providing the angle between the inner and outer set of flexures as indicated in Fig. 5. Considering a realistic value of  $\lambda = 1.1$  combined with feasible values of  $\alpha_1$  and  $\alpha_2$  which allow for  $30^\circ$  deflection without interference between the flexures, for example  $\alpha_1 = 35^\circ$  and  $\alpha_2 = 55^\circ$ , the resulting parasitic motion is  $L/682$ .

## 4. Numerical optimization

In order to select the most suitable hinge topology for the bearing suspension, the design of the cross-spring pivot, cartwheel hinge and butterfly hinge are optimized numerically.

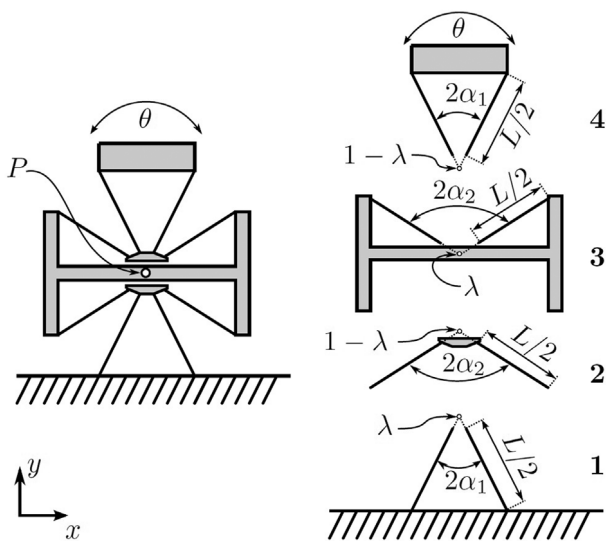


Fig. 5. Schematic overview of the butterfly hinge with P indicating the location of the (initial) pivot axis,  $\lambda$  the relative location at which the flexures cross and  $\theta$  the rotation angle of the shuttle.

#### 4.1. Optimization procedure

For the optimization procedure, an adapted Nelder–Mead based shape optimization algorithm [35] is used to optimize the length ( $L$ ) and thickness ( $t$ ) of the flexures to obtain maximum radial off-axis support stiffness. To obtain similar stiffness values in all radial directions, a value of  $\alpha = 45^\circ$  is selected for the cross-spring pivot and the cartwheel hinge ( $\alpha = 45^\circ$  can be considered optimal when maximizing the critical off-axis stiffness). For the butterfly hinge,  $\alpha_1 = 35^\circ$  and  $\alpha_2 = 55^\circ$  is selected, which is chosen as close to  $45^\circ$  as possible while still allowing for  $30^\circ$  deflection in each direction.

Furthermore, the minimum allowed flexure thickness is set at 0.2 mm, which is considered the minimum flexure thickness which can be manufactured (with sufficient accuracy) by wire EDM, which is the selected manufacturing method for the flexures. The length of the flexures ( $L$ ) is limited according to the provided equations in Section 3 in order to assure parasitic motion below 1 mm. Note that for the actual system a parasitic motion well below 1 mm is required in order to allow for additional deflection due to the reaction forces involved. However, for an initial comparison between the joints, we accept a parasitic motion up to 1 mm which provides maximum “design” freedom in the optimization procedure, resulting in the “best-case” off-axis support stiffness we can obtain with each of the flexure joints, which will be used for comparison.

For the optimization procedure, the performance is evaluated over the entire range of motion with the flexible multi-body software SPACAR [36] which uses a series of interconnected nonlinear 3D finite beam elements which include the geometric non-linearities to capture the relevant behavior of the flexures. The objective of the optimization is to maximize the radial support stiffness in the most compliant direction ( $K_{crit}$ ) over the range of motion of  $60^\circ$  ( $-30^\circ$  to  $+30^\circ$ ) with the goal to obtain sufficient resistance to pull-in and reaction forces. As material, tooling steel (Stavax) is selected where we limit the allowable stress to 600 MPa, which is about 40% of the yield stress of the material. Furthermore, the maximum width of the hinges is limited to 100 mm measured in the direction of the rotation axis.

#### 4.2. Optimization results

An overview of the optimization results is presented in Table 1, with each design just within the allowed stress limit of 600 MPa at their maximum deflection angle.

Table 1

Optimization results with the radial support stiffness ( $K_{crit}$ ) and parasitic motion ( $d$ ) provided at the maximum deflection angle of  $\theta = 30^\circ$ . (CP: Cross-spring Pivot; CFH: Cartwheel Flexure Hinge; BFH: Butterfly Hinge).

	CP	CP	CFH	BFH
$\lambda$	0.5	$\frac{1}{2} \pm \frac{\sqrt{5}}{6}$	–	1.1
$L$	[mm]	31	63	153
$t$	[mm]	0.27	0.20	0.42
$K_{crit}$	[N/mm]	1492	64	869
$d$	[mm]	0.98	0.09	0.94

From the results it can be confirmed that the cross-spring pivot with  $\lambda = 0.5$  requires short flexures in order to ensure parasitic motion below 1 mm, limiting the flexure length to 31 mm. Furthermore, this cross-spring pivot provides the highest level of support stiffness at the maximum deflection angle of 1492 N/mm. In contrast, the cross-spring pivot with  $\lambda = 1/2 \pm \sqrt{5}/6$  features a much smaller parasitic motion of only 0.09 mm, although it comes at the expense of a strongly reduced support stiffness (64 N/mm). Taking into account the negative stiffness induced by the rotor ( $-350$  N/mm), the obtained support stiffness is insufficient. The relatively low support stiffness can be related to its asymmetric design, resulting in high stress concentrations that require long and slender flexures to keep stress below 600 MPa.

The parasitic motion of the cartwheel flexure hinge is comparable with the cross-spring pivot with  $\lambda = 1/2$  while providing slightly less support stiffness (869 N/mm). At last, the butterfly hinge features a small magnitude for the parasitic motion combined with a relatively high support stiffness of 1283 N/mm.

#### 5. Influence of negative rotor stiffness

The numerically evaluated values for stiffness and parasitic motion discussed in the previous section do not take into account the additional pull-in forces due to parasitic motion of the rotor caused by the magnets. These magnetic forces are not included in the optimization procedure as it could result in buckling of the flexures during the static analysis of the flexure joints, which would result in problems with respect to convergence in numerical simulations due to its strongly non-linear behavior and possibly absence of a static equilibrium. Consequently, this lack of convergence would result in a great increase in the required computational effort for the optimization of the flexure joints.

To overcome this, the influence of these forces are excluded in the optimization procedure and analyzed separately in this section. The cross-spring pivot with  $\lambda = 1/2 \pm \sqrt{5}/6$  is not considered as the inherent support stiffness of this joint (64 N/mm at the maximum deflection angle) is already insufficient to counteract for the negative stiffness induced by the magnetic forces ( $-350$  N/mm).

To model the influence of the magnetic forces, a spring with negative stiffness is modeled between the shuttle of each flexure joint (the rotor) and the fixed world which captures the static load caused by the combination of negative stiffness and parasitic motion of the rotor. The spring is located at the initial location of the rotation axis of the flexure hinge, considering perfect initial alignment between the rotor and the stator (meaning zero reaction forces at  $\theta = 0^\circ$ ).

##### 5.1. Simulation results including negative rotor stiffness

For reference, the support stiffness without considering the negative rotor stiffness is provided in Fig. 6. Furthermore, the stiffness values and maximum Von Mises stress in the flexures including the negative rotor stiffness and the resulting reaction forces are provided in Figs. 7 and 8.

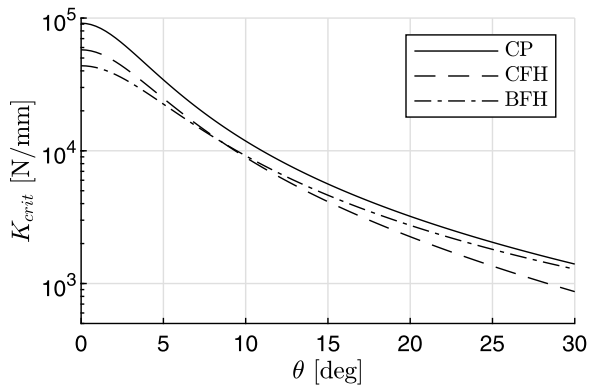


Fig. 6. Support stiffness without negative rotor stiffness (CP: Cross-spring Pivot, CFH: Cartwheel Flexure Hinge, BFH: Butterfly Hinge).

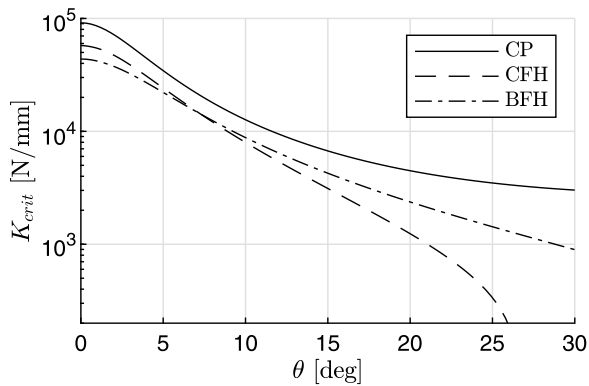


Fig. 7. Support stiffness with negative rotor stiffness (–350 N/mm) and reaction forces caused by parasitic motion included (CP: Cross-spring Pivot, CFH: Cartwheel Flexure Hinge, BFH: Butterfly Hinge).

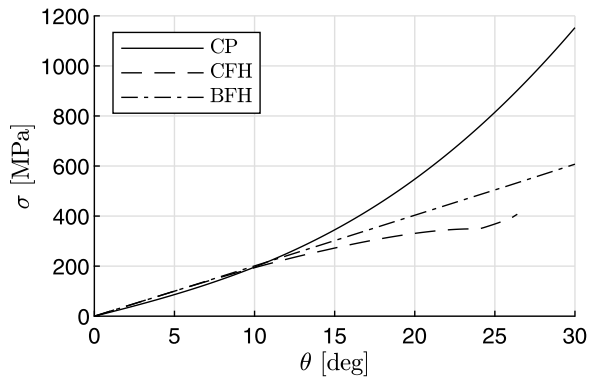


Fig. 8. Maximum stress (Von Mises) (CP: Cross-spring Pivot, CFH: Cartwheel Flexure Hinge, BFH: Butterfly Hinge).

From the results it can be observed that the reaction forces caused by the negative stiffness have a large influence in the observed off-axis stiffness and maximum stress in the flexures, especially when considering larger deflection angles. For the cartwheel flexure hinge, the reaction forces caused by parasitic motion (which is in the negative  $y$ -direction) result in large compressive loads in the flexures causing load softening [24,37]. Due to these forces, the flexures start to buckle at a deflection angle of  $\theta \approx 25^\circ$  at which the off-axis support stiffness deteriorates rapidly, resulting in insufficient stiffness to counteract the magnetic forces. Furthermore, the reaction forces result in a slight decrease in maximum stress due to the changed stress-distribution in the flexures. More specifically, the maximum stress in a cartwheel hinge

without load in the load bearing directions occurs at the intersection of the individual flexures (at the center of the joint). However, when the flexures are subjected to compressive loads, stress in the center of the joint decreases resulting in a reduced stress maximum, although stress increases at other locations in the flexures.

In contrast to the cartwheel hinge, parasitic motion of the cross-spring pivot is oriented in the positive  $y$ -direction, resulting in large tensile loads in the flexures. Due to the tensile loads, stress stiffening is observed resulting in an increase in off-axis support stiffness for the cross-spring pivot. Despite the increase in support stiffness in the cross-spring pivot, the high tensile load also results in an increased curvature of the flexures near the clamped ends. Therefore, stress is strongly increased (Fig. 8) up to almost 1200 MPa at the maximum deflection angle, which is an increase of about a factor of two.

For the butterfly hinge, support stiffness and the maximum stress in the flexures remains mostly unaffected by the additional reaction forces. Due to the small magnitude of the parasitic motion, the reaction forces are relatively small. Therefore, no excessive tensile or compressive loads occur in the flexures which would otherwise jeopardize its performance.

Overall, it can be concluded that the butterfly hinge is most suited for the rotor suspension, featuring low parasitic motion and high support stiffness in the off-axis directions. Furthermore, it is able to withstand the reaction forces induced by the rotor without suffering from a strong increase of stress in the flexures or a decrease of support stiffness due to compressive forces.

### 5.2. Load capacity

To further assess the performance of the butterfly hinge, the maximum load capacity of this joint is evaluated. This ultimate load capacity is defined as the load at which the parasitic deflection exceeds 1 mm (at the maximum deflection angle of 30 degrees), which results in contact between the rotor and the stator.

The maximum load capacity of the butterfly hinge is determined iteratively by gradually increasing load in the critical off-axis direction. Due to the magnetic pull-in forces in the direction of the parasitic motion, the off-axis stiffness in this direction is strongly reduced. Therefore, the critical most compliant off-axis direction is given by the direction of parasitic motion, which is in the vertical  $y$ -direction given by Eq. (7). Simulation results including this additional load is provided are Fig. 9, which take into account the negative rotor stiffness and contact between the rotor and stator. This simulation is conducted at a deflection angle of 30 degrees, providing the magnitude of the parasitic motion (*normal font*) and the support stiffness (*bold font*) as a function of the applied load.

From these results it can be concluded that the support stiffness decreases with increasing load, resulting in a support stiffness of about 100 N/mm at the maximum payload of 400 N (including the negative stiffness of –350 N/mm), resulting in contact between the rotor and the stator. It has to be noted that the stress in the flexures increases only slightly over a rather large displacement range of the rotor due to the decrement in support stiffness (the flexures are close to buckling), resulting in an increase of only 200 MPa when contact between the stator and rotor occurs. Therefore, excessive loads are rerouted through the frame parts without excessive stress levels exceeding the yield stress. This relieves the flexures and makes the system robust to extreme loading conditions. The 400 N of maximum load capacity provides a worst-case capacity at the maximum deflection angle. For smaller deflection angles, a load >400 N is allowed.

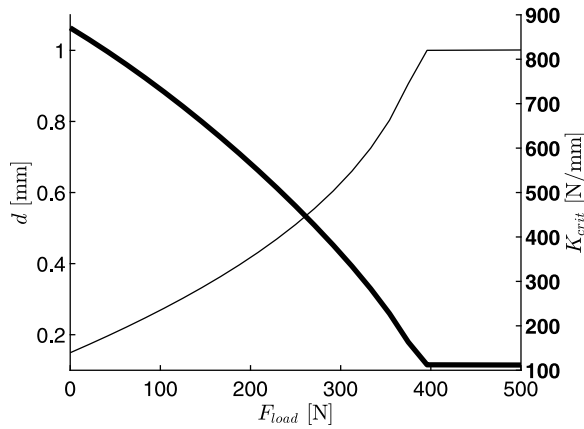


Fig. 9. Parasitic motion ( $d$ ) and critical off-axis support stiffness ( $K_{crit}$ ) of the butterfly hinge for increasing payload ( $F_{load}$ ) at the maximum deflection angle of  $\theta = 30^\circ$ .

## 6. Detailed design

Based on the optimization results, a prototype of the flexible actuator suspension for the selected torque motor is constructed by using the butterfly hinge design. The butterfly hinge is supplemented by a “slaving mechanism”, which is a flexure-based guidance for constraining the otherwise underconstrained intermediate body halfway the butterfly hinge [38]. The purpose of this slaving mechanism is to prevent low frequent vibrations of the large intermediate body halfway the butterfly hinge, which is unwanted for dynamics and control purposes. Note this guidance only provides significant stiffness in the underconstrained degree of freedom of the butterfly hinge and does not affect the off-axis support stiffness.

First, the detailed design of the actuator suspension is discussed in Section 6.1. Secondly, the controller design is discussed in Section 6.2.

### 6.1. Actuator suspension design

A photograph and a design drawing with exploded view of the designed prototype is provided in Figs. 10 and 11, which shows the suspension for two actuators with parallel rotation axes (rotor and flexure bearing only present for the actuator on the left-hand side). In the design, a butterfly hinge (1) with a width of 50 mm and slaving mechanism (2) are placed on each side of an aluminum rotor hub (3) which carries the permanent magnets of the rotor (4). By placing two butterfly hinges at each side of the rotor, high stiffness in both the translational and rotational load carrying directions are provided. The central “large” intermediate bodies which are constrained by the slaving mechanisms are interconnected with an aluminum body (5). This body is placed inside the rotor hub and provides a stiff connection between the intermediate slaved bodies. Furthermore, the rotation of the rotor is measured by a linear optical encoder (6) (Heidenhain’s LIC 4119 with a 1 nm measuring step), placed at a radius of 75 mm (resulting in a resolution of 13 nrad) which is able to maintain focus over the entire range of motion taking into account the parasitic motion of the rotor.

To reduce parasitic motion of the butterfly hinge and to reduce the stress in the flexures, the design of the butterfly hinge has been modified by splitting the large intermediate body in half, schematically illustrated in Fig. 12. Hereby, the flexures can be placed more closely to the instant center of rotation, reducing the values of  $\lambda$ , allowing for  $\lambda = 1.1$  which would not be possible otherwise. The two separate parts of the split intermediate body are connected to each other by means of a “rigid” part of the slaving mechanism, illustrated in Fig. 11.

In order to prevent excessive rotations, a mechanical stop (7) and optical switch (8) near the end of the range of motion are added to



Fig. 10. Photograph with the main dimensions of the flexure-based actuator suspension.

the rotor. The actuator’s stator (9), which is the stationary part of the actuator containing the coils, is fixed inside an aluminum frame (10). This frame holds the stator and improves the thermal dissipation for the current conducting coil. Furthermore, the housing is equipped with cooling channels (11) to provide active cooling to the stator for high load applications.

As two butterfly hinges at each side of the rotor are used for supporting the actuator, the system is overconstrained which could result in excessive stress, increased stiffness in the degree of freedom or even decreased stiffness in the support directions. Therefore, care is taken for the positioning of the two individual butterfly hinges ensuring good alignment between them. In particular the location of the rotation axis of both butterfly hinges requires proper alignment, which is ensured by using dowel pins for both hinges.

Furthermore, it has to be noted that insertion of the rotor during assembly requires special attention in order to provide resistance to the negative radial stiffness and to ensure good alignment between the stator and rotor. For this purpose, a linear guidance and a spacer for filling the air gap between the rotor and stator is used, which is removed after assembly.

### 6.2. Controller design

The absence of static friction allows accurate positioning, because no limit cycling will occur when using integral control action. On the other hand, the absence of self-locking friction makes the rotor position sensitive to disturbances and the combination with the rotational stiffness requires the controller to be active even after the target position is reached. The main source of disturbance is found to be the noise on the current introduced by the motor driver used to power the actuator, which is approximately white noise. Therefore, the transfer from the current noise to the position error (the input sensitivity) is minimized by H2 feedback control design [39]. The mechanics model for the control design is obtained from identification (see also Fig. 13). The H2 feedback control design is formulated as a mixed sensitivity control problem with the addition of a small scalar weight times the noise sensitivity. The small scalar makes the effect of the noise sensitivity negligible, such that the limit in minimizing the input sensitivity is imposed by the communication delays between the real-time system and the motor driver. Tracking will be improved by model-based feed-forward of dynamic forces, which can be predicted accurately due to the deterministic behavior of the mechanics.

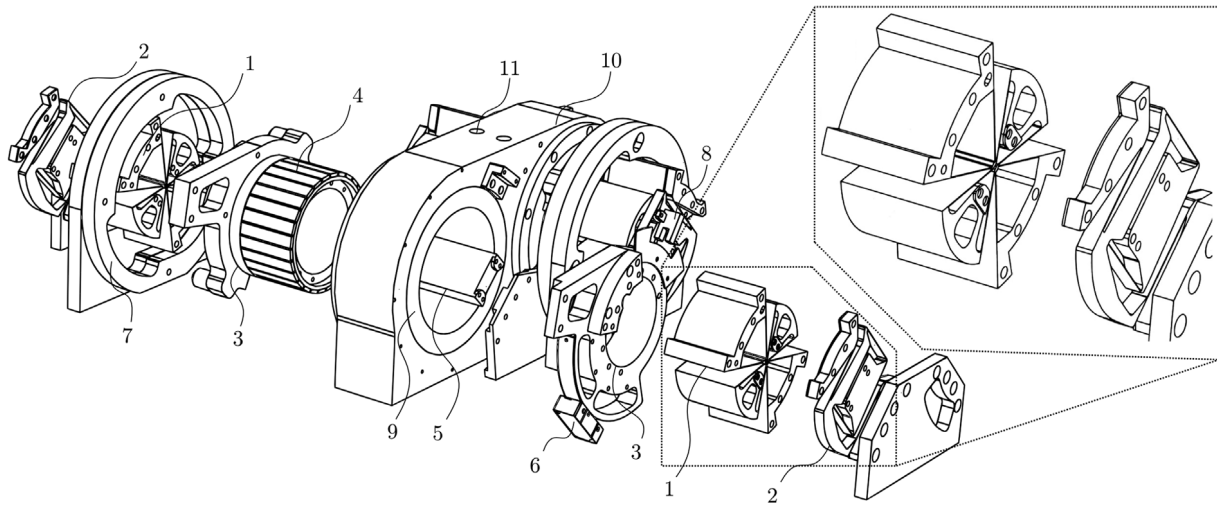


Fig. 11. Exploded view of actuator suspension. (1) Butterfly hinge (2) Slaving mechanism (3) Rotor-hub (4) Permanent magnets of the rotor (5) Body coupling intermediate bodies of both butterfly hinges (6) Encoder (7) Mechanical stop (8) Optical switch (9) Actuator's stator (10) Stator housing (11) Cooling channels.

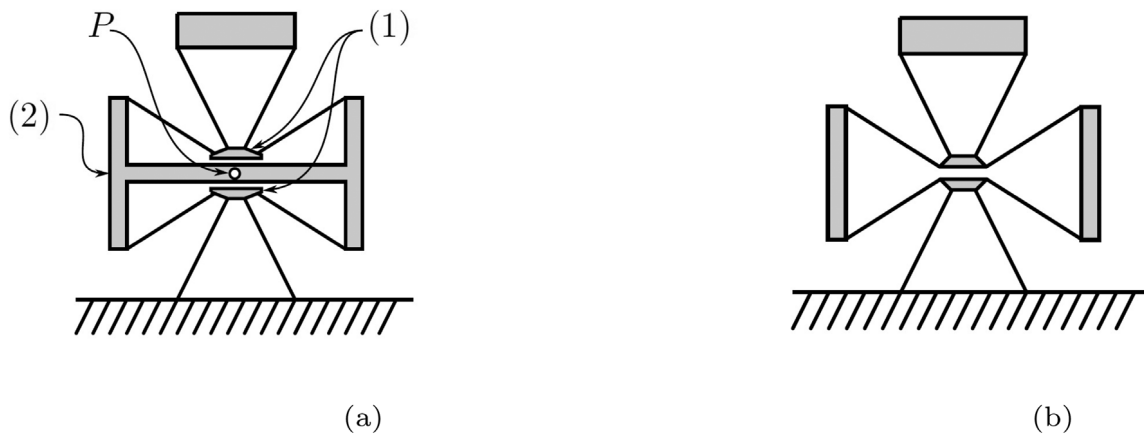


Fig. 12. (a) Schematic overview of a butterfly hinge with: (1) small intermediate body with high natural frequency (2) large intermediate body with low natural frequency (b) Schematic overview of butterfly hinge with separated intermediate body.

## 7. Experimental validation

### 7.1. Parasitic motion

To confirm the small magnitude of parasitic motion for the butterfly hinge, the encoder (Fig. 11, part number 7) is replaced by a capacitive displacement sensor (Lion Precision C6, range: 500  $\mu\text{m}$ , accuracy: < 0.1  $\mu\text{m}$ ) mounted perpendicular to the cylindrical rotor surface of the sensor strip. The displacement sensor is positioned at this location as the axis drift is maximum in the direction perpendicular to the symmetry axis of the butterfly hinge (the  $x$ -direction as indicated in Fig. 5), which is at the location of the encoder. Furthermore, the part of the rotor to which the sensor strip is attached is the only cylindrical surface that is accessible over the full range of motion of 60 degrees of rotation.

Measuring the relative displacement of the rotor over the range of motion includes the combined effect of the parasitic motion of the butterfly hinges (simulated value: 0.1 mm), lateral displacement caused by misalignment of the rotor with respect to the rotation axis of the butterfly hinges (eccentricity) and displacement caused by the limited circularity of the reference surface due to manufacturing tolerances. In order to minimize the eccentricity, the butterfly hinges are positioned by dowel pins with a positioning tolerance <20  $\mu\text{m}$ . Combined with the bi-directional range of motion of 30 degrees, the lateral displacement caused by eccentricity is <2  $\mu\text{m}$ . Furthermore, the reference surface

used for the displacement sensor is manufactured by CNC milling within a tolerance of approximately 10  $\mu\text{m}$ . Overall, the combined effect of eccentricity and manufacturing tolerances is estimated at <12  $\mu\text{m}$ , which is about 10% of the expected axis drift caused by the deflection of the butterfly hinges.

The total measured displacement of the rotor with respect to its neutral position is -0.09 mm at -30° rotation and 0.11 mm at +30° rotation. Taking into account deviations caused by eccentricity and manufacturing tolerances, the magnitude of the parasitic displacement is in line with the simulated values and confirm the ability of the butterfly hinges to maintain the position of the rotation axis in the center of the rotor, including the magnetic forces induced by the rotor.

It has to be noted that the measured (and simulated) values for the parasitic motion are highly repeatable and do not affect the repeatability of the overall system.

### 7.2. Support stiffness

To validate the support stiffness of the rotor suspension, the frequency of the first parasitic vibration mode of the end-effector is evaluated, which is directly related to the (critical) radial support stiffness. This parasitic vibration mode consists of a translational radial motion approximately parallel to the encoder head on the rotor-hub, which can be detected by the encoder. To determine the stiffness, the

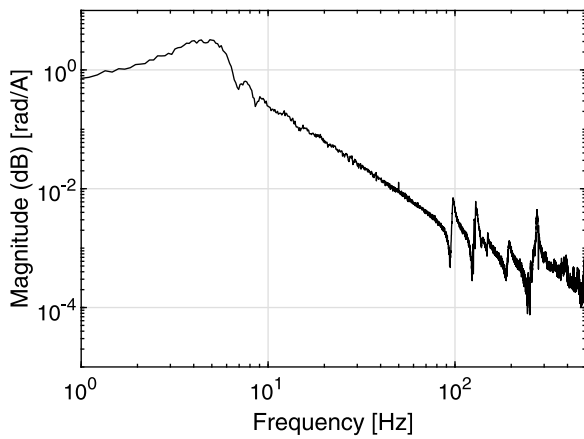


Fig. 13. Transfer function from current (A) to rotor position (rad) at  $\theta = 25^\circ$ .

frequency response from actuator current to rotation of the rotor is evaluated, which is provided in Fig. 13. This frequency response is evaluated close to the maximum deflection angle while still allowing for sufficient range of motion for a sweep signal on the input current. From this data, the first (damped) eigenfrequency in the degree of freedom of the system can be observed at about 5 Hz. At 98 Hz, the first parasitic eigenfrequency can be observed which can be related to the off-axis support stiffness of the system. In combination with the 3.0 kg mass of the end-effector, consisting of the rotor, rotor-hub and a part of the butterfly hinges, this provides a radial support stiffness of approximately 1138 N/mm. This is in good agreement with simulations and confirms the intended high radial stiffness of the butterfly hinges (simulated value  $K_{crit} \approx 1400$  N/mm at  $\theta = 25^\circ$ , Fig. 7). The slightly lower stiffness values in the measurement can be related to additional compliance of the frame parts, which are disregarded in the simulations.

### 7.3. Load capacity

To validate the load capacity, an additional off-centered mass (solid block of aluminum) is attached to the rotor of which the inertia is equivalent to the load in the considered application. This increase of load results in a total inertia of 0.066 kgm<sup>2</sup> with respect to the rotation axis and a mass of 4.4 kg with the center of mass located at 65 mm from the axis of rotation.

The load capacity is validated by accelerating the mass up to 400 rad/s<sup>2</sup>, resulting in reaction forces of approximately 115 N in the radial direction, which is of comparable magnitude as the expected reaction forces in the hexapod application. The measured position and acceleration is presented in Fig. 14. Visual inspection of the rotor suspension during the tests show no failure or parasitic deformations which indicate that the actuator suspension is able to withstand the high reaction forces involved. Furthermore, the system has been disassembled and inspected after experiments, showing no signs of damage or contact between the rotor and stator.

### 7.4. Repeatability

As the system is free of play and friction (and therefore free of self-locking and limit cycling), the repeatability of the system is directly determined by the stand-still performance of the system. To test the repeatability, the rotor is moved to a setpoint while the positioning error is tracked. For the presented case, the rotor is moved from  $\theta = -22.5^\circ$  to  $\theta = -2.5^\circ$  in 0.2 s. The resulting error for a single movement is provided in Fig. 15 where motion starts at  $t = 0$  s. Furthermore, a more detailed view of the position of the rotor between  $t = 2$  and  $t = 2.5$  s is provided in Fig. 16.

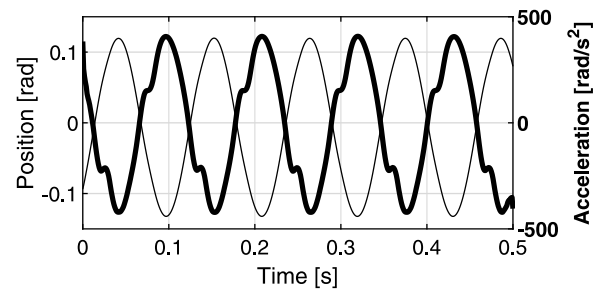


Fig. 14. Measured position and acceleration of the rotor during load capacity tests. The ripple in accelerations is caused by cogging forces of the actuator (no feedforward/cogging compensation is active during this experiment).

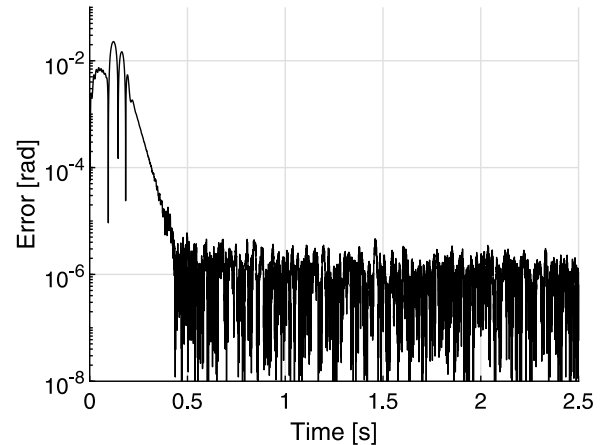


Fig. 15. Position error for tracking a reference signal moving from  $\theta = -22.5^\circ$  ( $t = 0$ ) to  $\theta = -2.5^\circ$  ( $t = 0.2$ ).

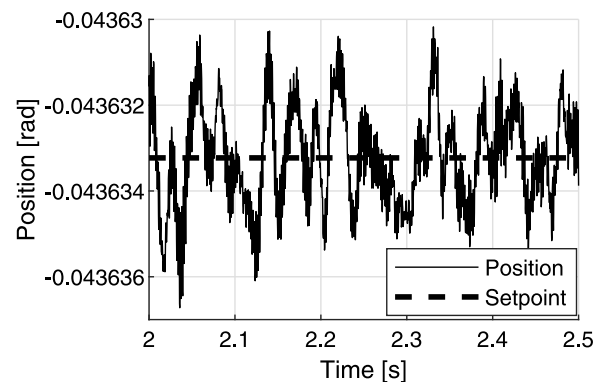


Fig. 16. Position of the end-effector from  $t = 2$  to  $t = 2.5$  s.

From the results it can be observed that the position of the rotor has converged to the target position in about 0.5 s, after which it fluctuates around the target position with an average error of 1.1  $\mu$ rad RMS. These fluctuations in the position are caused by current fluctuations (current ripple) from the motor driver ( $\pm 5$  mA RMS noise), resulting in deviations in the generated torque (motor constant 5.57 Nm/A). As stated earlier, due to the absence of friction, no stick-slip behavior is present in the flexure-based bearing suspension resulting in no mechanical resistance to small current (torque) variations. Therefore, small fluctuations in the provided current directly causes positioning errors of the rotor producing a vibrating motion around the reference position. The driver can be identified as the source of this error as these fluctuations are only present when the motor driver is active.

## 8. Discussion

With the tested system a repeatability of 1.1  $\mu\text{rad}$  RMS is obtained which is limited by the electronics. In order to reduce positioning errors, several solutions are suggested.

The most straight-forward solution is obtained by reducing the magnitude of the current noise caused by the motor driver. The currently used motor driver has a typical noise level for well-designed commercial motor drivers. Further reducing the output noise would require a dedicated motor driver design, which is costly (especially) considering the high power requirements for the considered actuator. Alternatively, instead of reducing the current noise levels, the sensitivity of the rotor position with respect to current deviations can be reduced. This can be achieved by increasing the total inertia of the system or by reducing the motor constant of the actuator (i.e. selecting a different actuator). However, both solutions reduce the maximum acceleration of the system, with the ratio between maximum acceleration and sensitivity with respect to current noise unchanged.

This ratio can be improved by increasing inertia by means of a counter-mass to balance the weight of the lower arm attached to the rotor (the lower arm in the hexapod application, Fig. 1). As the counter-mass compensates for torque required to counteract gravity, less torque is required to maintain a stationary position preserving more torque for accelerating. Furthermore, it results in a more favorable equilibrium position at approximately  $0^\circ$  rotation of the rotor (instead of the equilibrium position beyond  $-30^\circ$ , touching the mechanical end stop). At last, balancing results in a location of the center of mass closer to the axis of rotation of the rotor, reducing the radial reaction forces involved with high accelerations.

For the considered hexapod, fully balancing the static forces (exactly balanced at its neutral position) is feasible by adding a 2.5 kg counterweight to the rotor. This counterweight would result in approximately twice the effective inertia observed at the actuator, halving the positioning error below 0.6  $\mu\text{rad}$  RMS.

## 9. Conclusion

A high performance flexure-based suspension for an iron core direct drive torque motor with high radial support stiffness and high load capacity has been designed. The system allows for a 60 degrees range of motion combined with an ultimate torque of 55 Nm and features high repeatability. The repeatability is measured at 1.1  $\mu\text{rad}$  RMS positioning error with a load of 0.066  $\text{kgm}^2$ , at present limited by electronics.

For the actuator suspension, a butterfly hinge has been optimized, resulting in only 0.1 mm parasitic radial displacement over the range of motion, which limits pull-in forces typical for iron core actuators. The radial support stiffness exceeds 1000 N/mm with a radial load capacity of 400 N at the maximum deflection angle. This provides adequate support stiffness to compensate for the magnetic reaction forces induced by the iron core of the actuator. Furthermore, due to the design of the actuator with a 1 mm air gap between the rotor and stator, the flexures are inherently protected from excessive radial loads by rerouting excessive force through the frame parts, relieving the flexures.

Experimental validations confirm the high support stiffness, load capacity and robustness and prove the applicability of a flexure-based suspension for high torque iron core actuators.

### Declaration of competing interest

The authors declare that they have no known competing financial interests or personal relationships that could have appeared to influence the work reported in this paper.

## Acknowledgments

This research was funded by the Innovative Research Incentives Scheme VIDII (Stichting voor de Technische Wetenschappen)(14152 NWO TTW) of the ministry of Education, Culture and Science of the Netherlands. The authors acknowledge the contribution from ir. Dave Vogel for the implementation of control and the conducting of experiments. The authors would also like to thank the following companies for their support and technical advice in this project; Tecnotion B.V., Almelo, The Netherlands; Heidenhain Netherlands B.V., Ede, Netherlands, SigmaControl B.V., Barendrecht, The Netherlands.

## References

- [1] Merlet JP. Parallel robots. Spring Science & Business Media; 2006. <http://dx.doi.org/10.1007/1-4020-4133-0>, arXiv:arXiv:1011.1669v3.
- [2] Pyschny NK. Auslegung und Optimierung von festkörpergelenkbasierten Parallelkinematiken für die Montage von optischen Komponenten (Ph.D. thesis), Rheinisch-Westfälischen Technischen Hochschule Aachen; 2014.
- [3] Physik Instrumente (PI). Hexapod positioning systems. 2019. [https://static.physikinstrumente.com/fileadmin/user\\_upload/physik\\_instrumente/files/CAT/PI-CAT136-Hexapod-Positioning-Systems.pdf](https://static.physikinstrumente.com/fileadmin/user_upload/physik_instrumente/files/CAT/PI-CAT136-Hexapod-Positioning-Systems.pdf). URL [https://static.physikinstrumente.com/fileadmin/user\\_upload/physik\\_instrumente/files/CAT/PI-CAT136-Hexapod-Positioning-Systems.pdf](https://static.physikinstrumente.com/fileadmin/user_upload/physik_instrumente/files/CAT/PI-CAT136-Hexapod-Positioning-Systems.pdf).
- [4] Smith DR, Souccar K, Gale DM, Lucero M, Hernández E, Olmos A, Moreno ME, Cuq M, Noire P, Pawlowski R, Roux T. Factory characterization testing of a large precision hexapod for the LMT/GTM. In: Advances in optical and mechanical technologies for telescopes and instrumentation III, Vol. 10706. 2018, 1070649. <http://dx.doi.org/10.1117/12.2311674>.
- [5] Bacher JP, Bottinelli S, Breguet JM, Clavel R. Delta 3 : design and control of a flexure hinge mechanism. In: Microrobotics and microassembly III, Vol. 4568. 2001, p. 135–42. <http://dx.doi.org/10.1117/12.444120>.
- [6] Feddema JT, Keller CG, Hower RT. Experiments in micromanipulation and CAD-driven microassembly. In: SPIE's intelligent systems and advanced manufacturing symposium: Microbotics and microsystem fabrication conference. Pittsburgh, 1997.
- [7] Hesselbach J, Wrege J, Raatz A, Becker O. Aspects on design of high precision parallel robots. *Assem Autom* 2004;24(1):49–57. <http://dx.doi.org/10.1108/01445150410517183>.
- [8] Smith ST. Flexures: Elements of elastic mechanisms. London: Taylor & Francis; 2000.
- [9] Howell LL. Compliant mechanisms. John Wiley & Sons; 2001.
- [10] Soemers H. Design principles for precision mechanisms, T-pointprint, enschede. 2010.
- [11] Cosandier F, Henein S, Richard M, Rubbert L. The art of flexure mechanism design. Epl Press; 2017.
- [12] Dong W, Sun L, Du Z. Stiffness research on a high-precision, large-workspace parallel mechanism with compliant joints. *Precis Eng* 2008;32(3):222–31. <http://dx.doi.org/10.1016/j.precisioneng.2007.08.002>.
- [13] Wu TL, Chen JH, Chang SH. A six-dof prismatic-spherical-spherical parallel compliant nanopositioner. *IEEE Trans Ultrason Ferroelectr Freq Control* 2008;55(12):2544–51. <http://dx.doi.org/10.1109/TUFFC.2008.970>.
- [14] Brecher C, Pyschny N, Behrens J. Flexure-based 6-axis alignment module for automated laser assembly. In: International precision assembly seminar. 2010, p. 159–66. [http://dx.doi.org/10.1007/978-3-642-11598-1\\_18](http://dx.doi.org/10.1007/978-3-642-11598-1_18).
- [15] SmarAct. SMARPOD 110. 45. 2019. <https://www.smaract.com/smarpod/product/smarpod-110-45>. URL <https://www.smaract.com/smarpod/product/smarpod-110-45>.
- [16] Timmer Arends JH, Voss KHJ, Hakvoort WBJ, Aarts RGKM. Kinematic calibration of a six DOF flexure-based parallel manipulator. In: ECCOMAS thematic conference on multibody dynamics. Prague, 2017. p. 199–211.
- [17] Wavre N, Thouvenin X. Voice-coil actuators in space. In: 6th European space mechanisms and tribology symposium, Vol. 374. 1995, p. 227.
- [18] Ferková Z, Franko M, Kuchta J, Rafajdus P. Electromagnetic design of ironless permanent magnet synchronous linear motor. In: International symposium on power electronics, electrical drives, automation and motion. 2008, p. 721–6. <http://dx.doi.org/10.1109/SPEEDHAM.2008.4581085>.
- [19] Ravaut R, Lemarquand G, Lemarquand V. Ironless permanent magnet motors: Three-dimensional analytical calculation. In: 2009 IEEE international electric machines and drives conference. 2009, p. 947–52. <http://dx.doi.org/10.1109/IEMDC.2009.5075318>.
- [20] Murugesan S. An overview of electric motors for space applications. In: IEEE transactions on industrial electronics and control instrumentation IEI-28. 1981, p. 260–5. <http://dx.doi.org/10.1109/TIECI.1981.351050>, (4).
- [21] Lathwaite ER, Nasar SA. Linear-motion electrical machines. In: Proceedings of the IEEE, Vol. 58. 1970, p. 531–40. <http://dx.doi.org/10.1109/PROC.1970.7692>.

- [22] Zelenika S, De Bona F. Analytical and experimental characterisation of high-precision flexural pivots subjected to lateral loads. *Precis Eng* 2002;26(4):381–8. [http://dx.doi.org/10.1016/S0141-6359\(02\)00149-6](http://dx.doi.org/10.1016/S0141-6359(02)00149-6).
- [23] Brouwer DM, Meijaard JP, Jonker JB. Large deflection stiffness analysis of parallel prismatic leaf-spring flexures. *Precis Eng* 2013;37(3):505–21. <http://dx.doi.org/10.1016/j.precisioneng.2012.11.008>.
- [24] Nijenhuis M, Meijaard JP, Brouwer DM. A spatial parametric model for the nonlinear stiffness characteristics of flexure strips. In: ASME 2018 international design engineering technical conferences and computers and information in engineering conference, Quebec City, 2018.
- [25] Van Eijk J. On the design of plate-spring mechanisms (Ph.D. thesis), Delft University of Technology; 1985, URL [http://repository.tudelft.nl/assets/uuid:a343fbc0-dd0d-4d8c-bd6e-4a85a53a8c5a/TR-diss-0001431\(1\).pdf](http://repository.tudelft.nl/assets/uuid:a343fbc0-dd0d-4d8c-bd6e-4a85a53a8c5a/TR-diss-0001431(1).pdf).
- [26] Haringx JA. The cross-spring pivot as a constructional element. *Flow Turbul Combust* 1949;1(1):313–32. <http://dx.doi.org/10.1007/BF02120338>.
- [27] Naves M, Aarts R, Brouwer D. Large stroke high off-axis stiffness three degree of freedom spherical flexure joint. *Precis Eng* 2019;56:422–31. <http://dx.doi.org/10.1016/j.precisioneng.2019.01.011>.
- [28] Tecnotion. Frameless torque motor series. 2018, <https://www.tecnotion.com/downloads/catalogue-torque.pdf>. URL <https://www.tecnotion.com/downloads/catalogue-torque.pdf>.
- [29] Tecnotion. Torque motor manual. 2018, <https://www.tecnotion.com/downloads/torque-motors-manual.pdf>. URL <https://www.tecnotion.com/downloads/torque-motors-manual.pdf>.
- [30] Pei X, Yu J, Zong G, Bi S, Su H. The modeling of cartwheel flexural hinges. *Mech Mach Theory* 2009;44(10):1900–9. <http://dx.doi.org/10.1016/j.mechmachtheory.2009.04.006>.
- [31] Henein S, Spanoudakis P, Droz S, Myklebust L, Onillon E. Flexure pivot for aerospace mechanisms. In: 10th European space mechanisms and tribology symposium. San Sebastian, Spain. 2003. p. 285–88.
- [32] Wittrick WH. The properties of crossed flexure pivots, and the influence of the point at which the strips cross. *Aeronaut Q* 1951;2(4):272–92. <http://dx.doi.org/10.1017/S0001925900000470>.
- [33] Hongzhe Z, Shusheng B. Accuracy characteristics of the generalized cross-spring pivot. *Mech Mach Theory* 2010;45(10):1434–48. <http://dx.doi.org/10.1016/j.mechmachtheory.2010.05.004>, URL <http://dx.doi.org/10.1016/j.mechmachtheory.2009.10.001>.
- [34] Shusheng B, Hongzhe Z, Jingjun Y. Modeling of a cartwheel flexural pivot. *J Mech Des* 2009;131(6). 061010. <http://dx.doi.org/10.1115/1.3125204>.
- [35] Naves M, Brouwer D, Aarts R. Building block-based spatial topology synthesis method for large-stroke flexure hinges. *J Mech Robot* 2017;9(4). 041006. <http://dx.doi.org/10.1115/1.4036223>.
- [36] Jonker J, Meijaard J. SPACAR — Computer program for dynamic analysis of flexible spatial mechanisms and manipulators. In: *Multibody systems handbook*. Berlin, Heidelberg: Springer; 1990, p. 123–43. [http://dx.doi.org/10.1007/978-3-642-50995-7\\_9](http://dx.doi.org/10.1007/978-3-642-50995-7_9).
- [37] Awtar S, Slocum A, Sevincer E. Characteristics of beam-based flexure modules. *J Mech Des* 2007;129(6):625. <http://dx.doi.org/10.1115/1.2717231>.
- [38] Henein S. Flexure delicacies. *Mech Sci* 2012;3:1–4. <http://dx.doi.org/10.5194/ms-3-1-2012>.
- [39] Kwakernaak H. H2-optimization - theory and applications to robust control design. *IFAC Proc Vol* 2000;33(14):437–48. [http://dx.doi.org/10.1016/S1474-6670\(17\)36268-7](http://dx.doi.org/10.1016/S1474-6670(17)36268-7).